REPORTS IN METEOROLOGY AND OCEANOGRAPHY
UNIVERSITY OF BERGEN 1-2011

A two-layer model for linear stability analysis of shelf-slope currents.

By

Sigurd Henrik Teigen

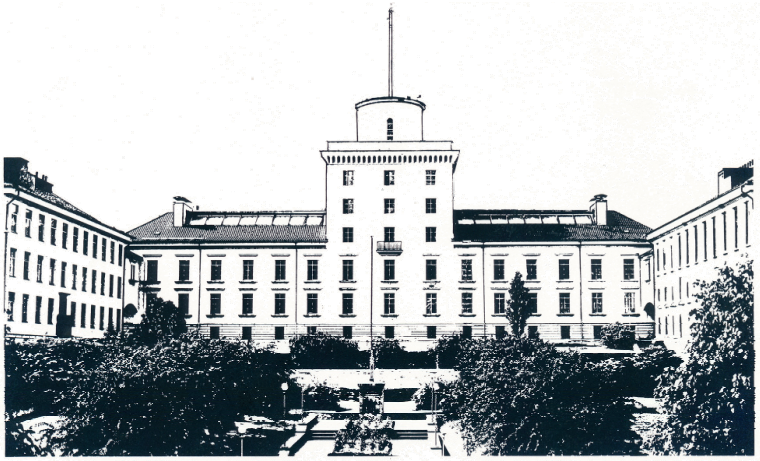

UNIVERSITY OF BERGEN

Geophysical Institute
Allégaten 70
5007 Bergen
Norway

Reports in Meteorology and Oceanography,
University of Bergen
Report no. 1-2011
ISSN 1502-5519
ISBN 82-8116-017-9

A two-layer model for linear stability analysis of shelf-slope currents

S. H. Teigen[1]
The University Centre in Svalbard
Longyearbyen
Norway

Abstract

A method for obtaining the normal mode solution of a linear two-layer system over sloping topography has been derived and implemented, providing a basic tool for analysing the dispersion relation and modal structure of stable and unstable baroclinic shelf waves. Model results are compared with analytical solutions for a step-shelf profile with no background flow and a linearly sloping channel with flow in both layers. A case study for the West Spitsbergen Shelf topography is also presented.

1 Introduction

Charney [1947] and Eady [1949] were the first to provide a mathematical treatment of the fundamental mechanisms of baroclinic instability in the context of geophysical fluid dynamics. From the very beginning, two-layer models have been useful concepts for exploring the basic dynamics of baroclinic instability [Phillips, 1954]. Semi-circle theorems and stability criteria for two-layer flows were exposed by Pedlosky [1963]. In [Pedlosky, 1964a,b] these were expanded to account for continuous stratification as well. Orlanski [1969] used a two-layer model with sloping topography to show that baroclinic instability is a probable source of energy for Gulf stream eddies offshore the east coast of the United States. Gill *et al.* [1974] demonstrated how potential energy in the mean circulation of the world oceans can be converted to eddy kinetic energy by baroclinic instability. Smith [1976] applied a two-layer channel model to investigate baroclinic instability in the Denmark Strait overflow, detecting similar oscillation periods in observational data as given by the model. A related model was used by Mysak and Schott [1977] to explain low-frequency oscillations in the Norwegian Atlantic Current. Flierl [1978] derived methods for optimal fitting of data to a two-layer model for oceanic applications. Mysak [1980] provided a thorough review of shelf wave theory and the two-layer models used therein for studying baroclinic effects. In [Mysak *et al.*, 1981], both baroclinic and barotropic instabilities are discussed for a two-layer model with a linear shelf and slope. Three-layer models have been applied to study a deep ocean with an upper current [Ikeda, 1983; Pichevin, 1998]. Poulin and Flierl [2005] systematically investigated the effect of prograde and retrograde topography for a two-layer model with a passive layer, finding that retrograde (with

[1]E-mail: sigurdt@unis.no, Phone: +47 79 02 33 53

the shallow water to the left) topography is always stabilizing, while prograde topography (with the shallow water to the right) can be either stabilizing or de-stabilizing, depending on the Rossby number and the amplitude of the topography under consideration. More recent papers focus on baroclinic instability as a source of eddy activity in the ocean [Smith, 2007; Ferrari and Wunsch, 2009] and attempts have been made to utilize linear models to parameterize the process for global ocean simulations [Isachsen, 2010].

The West-Spitsbergen Current (WSC) is an eastern boundary current flowing along the West Spitsbergen Slope (WSSl), and the main supplier of oceanic heat and salt for the Arctic Ocean. The WSC is renown for its frequent mesoscale eddying [Johannessen *et al.*, 1987; Gascard *et al.*, 1995]. Isopycnal diffusion of heat by eddy fields has been postulated as a vital process for cooling the subsurface layers of the current [Boyd and D'Asaro, 1994; Nilsen *et al.*, 2006; Teigen *et al.*, 2010], and unstable baroclinic wave modes constitute a source mechanism for these eddies. The present study describes a two-layer shallow-water linear model for stability analysis of shelf-slope currents, which has been developed with the aim of studying the properties and prevalence of unstable modes in the baroclinic WSC branch. A related barotropic model has been used with success to study stable and unstable barotropic shelf waves [Davies *et al.*, 2003; Thiem *et al.*, 2006; Nilsen *et al.*, 2006; Teigen *et al.*, 2010]. Although many general results have been obtained with the two-layer models that have been an integral ingredient in the study of baroclinic instability for more than 50 years, the detailed structure of the baroclinic wave modes is very sensitive to the topography and background density and current fields. For this reason it was practical to establish a numerical model that could handle a whole range of different current and topographic profiles, relevant for the WSC and the WSSl. The outline of the report is as follows, in section 2, the derivation of the linear two-layer model is presented, along with a semi-circle theorem and an instability criterion for two-layer models. In section 3, the numerical grid discretization and boundary conditions are presented. Sections 4.1 and 4.2 compares the model with analytical results, while section 4.3 deals with a practical application of the model to the WSC. Finally, in section 5 some summarizing remarks are given.

2 Theory

In a former study by Gjevik [2002], the matrix equation for the normal modes of a two-layer shallow-water system (see Figure 1) with no background flow in the lower layer was derived. Here, the model is generalized to allow for a non-zero flow in the lower layer as well. Subindices 1 and 2 refer to variables in the upper and lower layers, respectively. The u-component is pointing east towards the shore, while the v-component is in the along-shelf direction (pointing north along isobaths).

We assume a steady, along-slope, geostrophically balanced background current. Upon integration this yields for the displacement of the surface $\bar{\eta}_1$

$$\bar{\eta}_1 = -\frac{f}{g}\int_x^{L_x} \bar{v}_1 \mathrm{d}x, \tag{1}$$

where f is the Coriolis parameter, g is the acceleration of gravity, L_x is the total width of the channel and $\bar{v}_1(x)$ is the steady along-slope background current in the upper layer. For the displacement of the interface between the two layers, $\bar{\eta}_2$, we have

$$\bar{\eta}_2 = -\frac{f}{g'}\int_x^{L_x} \bar{v}_2 \mathrm{d}x - \frac{g\bar{\eta}_1}{g'}, \tag{2}$$

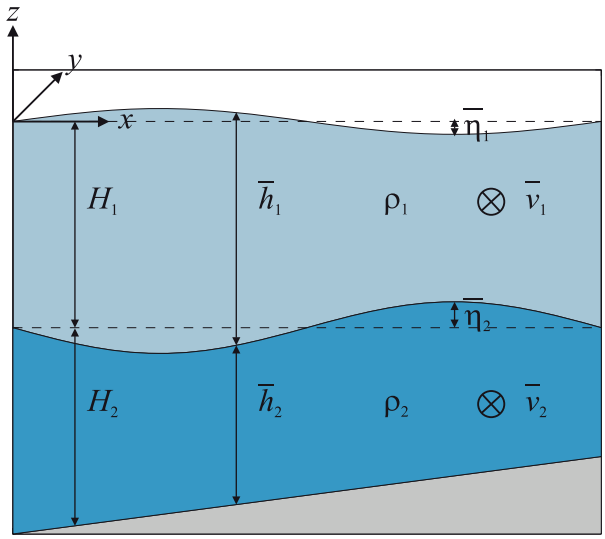

Figure 1: Illustration of definitions for the two layer model.

where $\bar{v}_2(x)$ is the background current in the lower layer and $g' = g\frac{\rho_2-\rho_1}{\rho_2}$ [m/s^2] is reduced gravity (ρ_1 and ρ_2 are the densities in the two layers).

The basis for the model is the depth-integrated shallow water equations. For the upper layer the equations of motion (3a, 3b) and the continuity equation (3c) are

$$\frac{\partial u_1}{\partial t} + u_1\frac{\partial u_1}{\partial x} + v_1\frac{\partial u_1}{\partial y} - fv_1 = -g\frac{\partial \eta_1}{\partial x} \tag{3a}$$

$$\frac{\partial v_1}{\partial t} + u_1\frac{\partial v_1}{\partial x} + v_1\frac{\partial v_1}{\partial y} + fu_1 = -g\frac{\partial \eta_1}{\partial y} \tag{3b}$$

$$\frac{\partial \eta_1}{\partial t} = -\frac{\partial}{\partial x}[u_1h_1 + u_2h_2] - \frac{\partial}{\partial y}[v_1h_1 + v_2h_2]. \tag{3c}$$

Here, h_1 is the total thickness of the upper layer (the mean thickness is $\bar{h}_1 = H_1 + \bar{\eta}_1 - \bar{\eta}_2$, H_1 is the thickness of the upper layer in the absence of a mean current) and h_2 is the total thickness of the lower layer (the mean thickness is $\bar{h}_2 = H_2 + \bar{\eta}_2$, H_2 is the thickness of the lower layer in the absence of a mean current). The density interface between the two layers may intersect the bottom topography, resulting in an offshore two-layer region and an onshore mono-layer region [Kawabe, 1982]. Offshore of the intersection point, $H_1 = d$ (d is the undisturbed interface depth) and $H_2 = h(x) - d$ ($h(x)$ is the undisturbed total depth), whereas in the mono-layer region, $H_2 = 0$

and $H_1 = h(x)$. In the lower layer, we have

$$\frac{\partial u_2}{\partial t} + u_2\frac{\partial u_2}{\partial x} + v_2\frac{\partial u_2}{\partial y} - fv_2 = -\frac{\partial}{\partial x}[g\eta_1 + g'\eta_2], \tag{4a}$$

$$\frac{\partial v_2}{\partial t} + u_2\frac{\partial v_2}{\partial x} + v_2\frac{\partial v_2}{\partial y} + fu_2 = -\frac{\partial}{\partial y}[g\eta_1 + g'\eta_2], \tag{4b}$$

$$\frac{\partial \eta_2}{\partial t} = -\frac{\partial}{\partial x}[u_2 h_2] - \frac{\partial}{\partial y}[v_2 h_2]. \tag{4c}$$

We introduce small perturbations to the background flow, according to

$$\eta_1 = \bar{\eta}_1 + \eta_1', \tag{5a}$$
$$u_1 = u_1', \tag{5b}$$
$$v_1 = \bar{v}_1 + v_1', \tag{5c}$$
$$\eta_2 = \bar{\eta}_2 + \eta_2', \tag{5d}$$
$$u_2 = u_2', \tag{5e}$$
$$v_2 = \bar{v}_2 + v_2'. \tag{5f}$$

The total layer thicknesses are now $h_1 = H_1 + \bar{\eta}_1 + \eta_1' - (\bar{\eta}_2 + \eta_2')$ and $h_2 = H_2 + \bar{\eta}_2 + \eta_2'$. In Equations 5a to 5f, primed quantities are perturbations. We search for normal modes on the form

$$\eta_1' = \hat{\eta}_1(x)\cos(ky - \omega t), \tag{6a}$$
$$u_1' = \hat{u}_1(x)\sin(ky - \omega t), \tag{6b}$$
$$v_1' = \hat{v}_1(x)\cos(ky - \omega t), \tag{6c}$$
$$\eta_2' = \hat{\eta}_2(x)\cos(ky - \omega t), \tag{6d}$$
$$u_2' = \hat{u}_2(x)\sin(ky - \omega t), \tag{6e}$$
$$v_2' = \hat{v}_2(x)\cos(ky - \omega t), \tag{6f}$$

where t is time, k is wave number and ω is angular velocity. Inserting the normal modes into the linearized versions of Equations 3a to 3c and 4a to 4c, leads to (after some algebra) the following matrix equation

$$\begin{Bmatrix} \bar{v}_1 k, & -\bar{h}_1\frac{\mathrm{d}}{\mathrm{d}x} - \frac{\mathrm{d}\bar{h}_1}{\mathrm{d}x}, & \bar{h}_1 k, & (\bar{v}_2 - \bar{v}_1)k, & -\bar{h}_2\frac{\mathrm{d}}{\mathrm{d}x} - \frac{\mathrm{d}\bar{h}_2}{\mathrm{d}x}, & \bar{h}_2 k \\ g\frac{\mathrm{d}}{\mathrm{d}x}, & \bar{v}_1 k, & -f, & 0, & 0, & 0 \\ gk, & -f - \frac{\mathrm{d}\bar{v}_1}{\mathrm{d}x}, & \bar{v}_1 k, & 0, & 0, & 0 \\ 0, & 0, & 0, & \bar{v}_2 k, & -\bar{h}_2\frac{\mathrm{d}}{\mathrm{d}x} - \frac{\mathrm{d}\bar{h}_2}{\mathrm{d}x}, & \bar{h}_2 k \\ g\frac{\mathrm{d}}{\mathrm{d}x}, & 0, & 0, & g'\frac{\mathrm{d}}{\mathrm{d}x}, & \bar{v}_2 k, & -f \\ gk, & 0, & 0, & g'k, & -f - \frac{\mathrm{d}\bar{v}_2}{\mathrm{d}x}, & \bar{v}_2 k \end{Bmatrix} \begin{Bmatrix} \hat{\eta}_1 \\ \hat{u}_1 \\ \hat{v}_1 \\ \hat{\eta}_2 \\ \hat{u}_2 \\ \hat{v}_2 \end{Bmatrix} = \omega \begin{Bmatrix} \hat{\eta}_1 \\ \hat{u}_1 \\ \hat{v}_1 \\ \hat{\eta}_2 \\ \hat{u}_2 \\ \hat{v}_2 \end{Bmatrix}, \tag{7}$$

which represents an eigenvalue problem for the complex frequency $\omega = \omega_r + \mathrm{i}\omega_i$. For $\omega_i > 0$, the solution is unstable with exponential growth rate ω_i. The real component ω_r determines the phase speed $c_r = \omega_r/k$ of the vorticity wave with wave period $P = 2\pi/\omega_r$ and wave length $\lambda = 2\pi/k$.

2.1 Semi-circle theorem and condition for instability

The complex phase speed $c = c_r + \mathrm{i}c_i$ of the unstable shelf waves resulting from arbitrary current and bathymetric profiles cannot be retrieved analytically. However, in many cases it is still possible

to obtain theoretical bounds on c_r and c_i. Pedlosky [1963] provides a semi-circle theorem for a flat-bottomed two-layer ocean, in analogy with Howard's famous semi-circle theorem for hydrodynamic instability [Howard, 1961], given by

$$\left(\frac{a-b}{2}\right)^2 \geq \left(c_r - \left(\frac{a+b}{2}\right)\right)^2 + c_i^2. \tag{8}$$

Here, a and b are the maximum and minimum current speed within the domain, in either of the two layers. From standard linear stability theory of quasi-geostrophic flows [Pedlosky, 1964a; Mysak *et al.*, 1981] a condition for exponential growth ($c_i > 0$) of a two-layer system with no horizontal shear ($\bar{v}_1, \bar{v}_2$ const.) and uniformly sloping topography can be derived

$$\frac{\bar{v}_1 - \bar{v}_2}{|\bar{v}_1 - c|^2}\int_0^{L_x} |\Phi_1|^2 \mathrm{d}x - \frac{\bar{v}_1 - \bar{v}_2}{|\bar{v}_2 - c|^2}\int_0^{L_x} |\Phi_2|^2 \mathrm{d}x - \frac{g'\alpha/f}{|\bar{v}_2 - c|^2}\int_0^{L_x} |\Phi_2|^2 \mathrm{d}x = 0, \tag{9}$$

where Φ_n $(n = 1, 2)$ is the complex amplitude in layer n of a normal mode unstable solution to the linearized quasi-geostrophic potential vorticity equation. α is the topographical slope. From this condition it can be seen that for strong slopes ($|\alpha|$ large) and/or strong stratification, the third term would dominate the others, rendering instability unlikely. However, if $\bar{v}_1 \approx c$ (for $\bar{v}_1 > \bar{v}_2$) or $\bar{v}_2 \approx c$ (for $\bar{v}_2 > \bar{v}_1$), the first or the second term will become large and could cancel the third term.

3 Numerical method

The lateral boundary condition at the walls ($x = 0$ and $x = L_x$) is zero normal velocity in both layers, i.e. $u'_n = 0, (n = 1, 2)$. For the case when the interface intersects the topography, the across-shelf velocity is zero at the intersecting grid point. A staggered one-dimensional grid was used for the numerical calculations (see illustration in Figure 2). The staggered grid discretization gives better accuracy than a collocated grid and the numerical boundary conditions are consistent with the analytical boundary conditions. The matrix system (7) was solved using `Matlab`, which utilizes the Lapack library routines for eigenvalue calculations. The modal structures of the real current and displacement fields is given by

$$u'_1 = [\hat{u}_{1,r}(x)\cos(ky - \omega_r t) - \hat{u}_{1,i}(x)\sin(ky - \omega_r t)]\exp(\omega_i t), \tag{10a}$$
$$v'_1 = [\hat{v}_{1,r}(x)\sin(ky - \omega_r t) + \hat{v}_{1,i}(x)\cos(ky - \omega_r t)]\exp(\omega_i t), \tag{10b}$$
$$\eta'_1 = [\hat{\eta}_{1,r}(x)\cos(ky - \omega_r t) - \hat{\eta}_{1,i}(x)\sin(ky - \omega_r t)]\exp(\omega_i t), \tag{10c}$$
$$u'_2 = [\hat{u}_{2,r}(x)\cos(ky - \omega_r t) - \hat{u}_{2,i}(x)\sin(ky - \omega_r t)]\exp(\omega_i t), \tag{10d}$$
$$v'_2 = [\hat{v}_{2,r}(x)\sin(ky - \omega_r t) + \hat{v}_{2,i}(x)\cos(ky - \omega_r t)]\exp(\omega_i t), \tag{10e}$$
$$\eta'_2 = [\hat{\eta}_{2,r}(x)\cos(ky - \omega_r t) - \hat{\eta}_{2,i}(x)\sin(ky - \omega_r t)]\exp(\omega_i t), \tag{10f}$$

where $\hat{u}_{n,r}, \hat{v}_{n,r}$ and $\hat{\eta}_{n,r}$ are the real components of the eigenvector in the n'th layer and $\hat{u}_{n,i}, \hat{v}_{n,i}$ and $\hat{\eta}_{n,i}$ are the imaginary components.

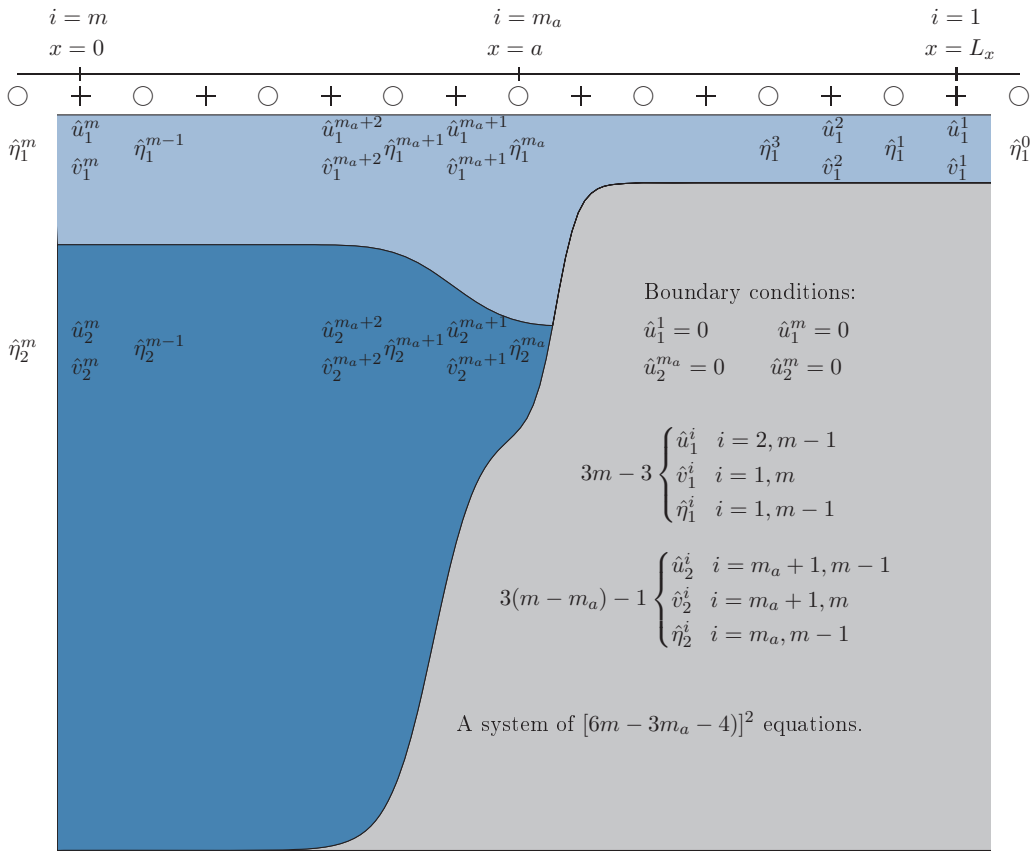

Figure 2: Illustration of the staggered grid discretization. Plus symbols denote nodes for $\hat{u}_n$ and $\hat{v}_n$, while circles mark nodes for $\hat{\eta}_n$.

4 Results

4.1 Comparison with step shelf

The step-shelf geometry is given by

$$h(x) = \begin{cases} h_o, & \text{for } 0 \leq x \leq l, \\ h_s, & \text{for } L_x \geq x > l, \end{cases} \tag{11}$$

where h_s is the depth on the shelf, h_o is the depth in the abyssal ocean and l is the position of the shelf-break (see illustration in Figure 3). With no background current, the following expression describing the relationship between ω and k can be derived analytically

$$(\omega - f)\left[h_2\left(\omega\frac{K}{k} - f\right) + h_1(\omega + f)\right] + \frac{h_2}{h_3}\left(\omega\frac{K}{k} - f\right)[h_1(\omega + f) + h_2(\omega - f)] = 0, \tag{12}$$

where $h_1 = h_s, h_2 = d$ and $h_3 = h_o - d$. $\frac{K}{k} = \sqrt{1 + \frac{f^2}{c_o^2 k^2}(1 - \frac{\omega^2}{f^2})}$, where $c_0 = \frac{g' h_1 h_3}{h_2 + h_3}$ is the internal gravity wave speed. The numerical two-layer model was run with parameter values similar to the West Spitsbergen Shelf (see Table 1).

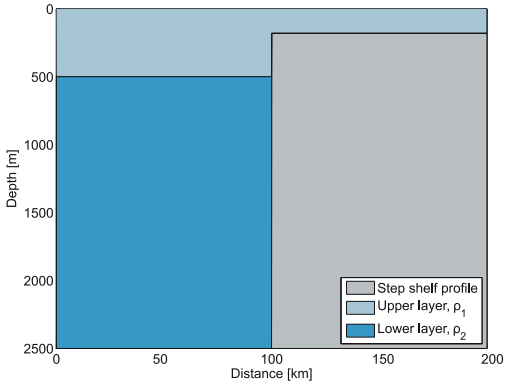

Figure 3: Illustration of the step-shelf profile and the two layers, for the parameter choices in Table 1.

Parameter	Value
h_s	180 m
h_o	2500 m
l	100 km
L_x	200 km
d	500 m
g'	$9.81 \cdot 10^{-3}$ m/s^2
f	$1.42 \cdot 10^{-4}$ s^{-1}

Table 1: Input parameters for the step shelf case.

The roots of equation 12 were found through numerical iteration, for a selection of wave lengths. A comparison with the dispersion relation found with the two-layer model can be seen in Figure 4. The match between the two models is quite close, the difference is barely discernable. For short wave lengths (20-80 km), the lowest mode follows the internal gravity wave period, while for longer wave lengths (beyond 80 km) the lowest mode approaches the inertial period. In Table 2, the convergence sequence for the highest mode can be seen for different grid sizes. The analytical solution for this wavelength ($\lambda = 50$ km) was $\omega/f = 0.437$ or $T = 28.53$ h. The results indicate that the present model comes quite close to the analytical solution for resolutions $\Delta x = 0.5$ km or less. The analytical solution is derived for an infinitely wide shelf and deep ocean, but increasing the width of the numerical calculation domain in the present model had little effect on the solution.

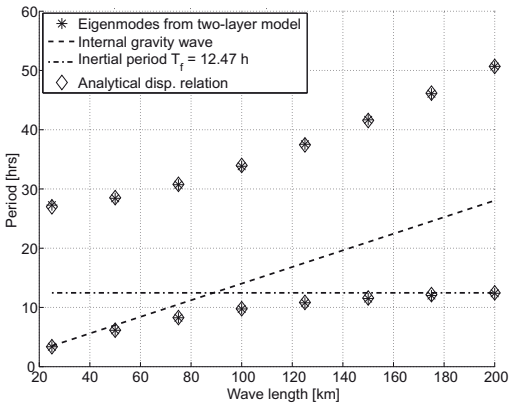

Figure 4: Comparison of the dispersion relation for the step-shelf topography (11) calculated with the numerical two-layer model and the analytical dispersion elation. The internal gravity wave and inertial wave periods are indicated.

Δx [km]	ω/f	T [hrs]
2	0.402	30.989
1	0.422	29.527
0.5	0.433	28.794
0.25	0.438	28.427

Table 2: Effect of grid refinement for a step shelf. The tabulated values are calculated for $\lambda =$ 50 km.

4.2 Comparison with linear slope profile [Mysak and Schott, 1977]

In a seminal paper on baroclinic instability in the Norwegian Atlantic Current (NAC), Mysak and Schott [1977] described in detail a quasi-geostrophic analytical model for calculation of the unstable baroclinic modes of a slope current in a two-layer system (with step-wise uniform current in the two layers), providing a suitable test case for comparison with the present numerical model. The linear slope profile is given by

$$h(x) = h_o - (h_o - h_s)x/L_x, \tag{13}$$

where h_s is the depth at the shoreward boundary of the channel and h_o is the depth at the offshore wall. The constant input parameters were similar to those of [Mysak and Schott, 1977], who used values relevant for the NAC at 63°N (see Table 3). The channel is illustrated in Figure 5.

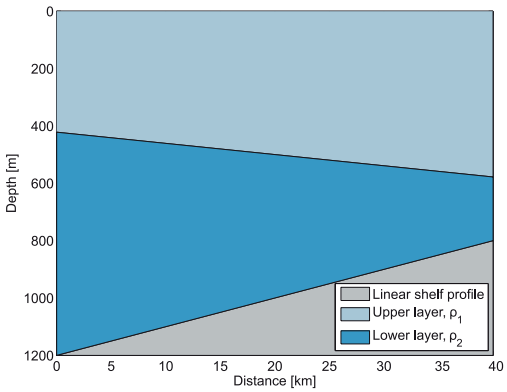

Figure 5: Illustration of the linear shelf profile and the two layers, for the parameter choices in Table 3.

Parameter	Value
h_s	800 m
h_o	1200 m
L_x	40 km
d	500 m
f	$1.3{\cdot}10^{-4}$ s^{-1}

Table 3: Input parameters for the linear slope case.

In Figure 6a-d the dispersion relation calculated with the present model and the model by [Mysak and Schott, 1977] is shown for two different values of reduced gravity and two different current shears between the layers. The similarity between the results obtained with the present model and those of [Mysak and Schott, 1977] is evident, although the growth rate is generally $\sim 5\%$ higher for their model. The long-periodic bands of stable modes display $\sim 5\%$ higher wave period for the model of Mysak and Schott [1977] in Figure 6a. For the other cases, the correspondence is better. One possible reason for the deviation between the two models is the fact that Mysak and Schott [1977] assume a rigid lid on top, while the present model retains a free surface. The surface divergence parameter $\frac{f^2 L_x^2}{g' d}$, which should be small for the rigid lid approximation to be justified, is decreasing with increasing stratification. This could explain why the correspondence is better for higher values of g'. The lowest stable mode in the present model is the internal gravity wave, and corresponds well with the analytical curve (Figure 6a-d). In Figure 6c a third peak in growth rate, which is not present in the solution by Mysak and Schott [1977] can be seen. It turns out that this mode is a combination of the first and the second mode which is not possible with the model by Mysak and Schott [1977].

Table 4: Detailed comparison with Mysak and Schott [1977]. γ is growth rate with unit [days^{-1}].

	MYSAK&SCHOTT			TWO-LAYER MODEL		
Case	T [hrs]	λ [km]	γ [days^{-1}]	T [hrs]	λ [km]	γ [days^{-1}]
Figure 6a	83.35	64	0.365	77.15	60	0.338
Figure 6b	99.73	90	0.116	97.99	88	0.112
Figure 6c	75.75	46	0.160	72.09	44	0.147
Figure 6d	80.91	54	0.047	78.52	52	0.043

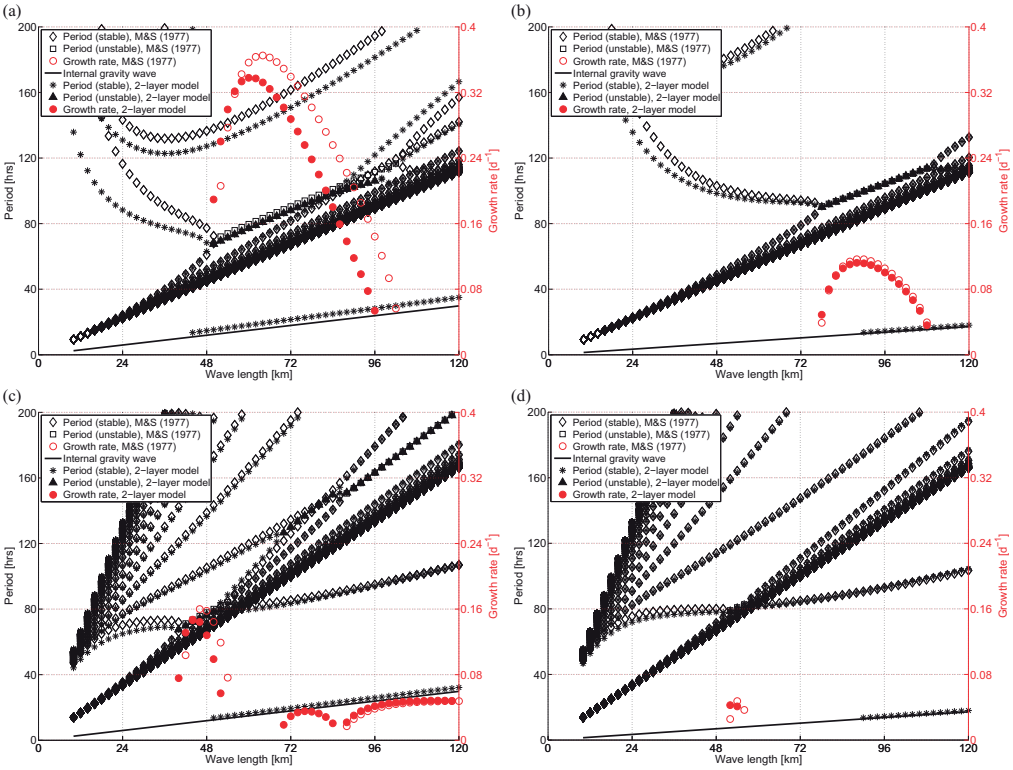

Figure 6: Comparison of the dispersion relation calculated with the model by Mysak and Schott [1977] and the present model . (a) $g' = 0.5 \cdot 10^{-2}$ m/s^2, $\bar{v}_1$=0.3 m/s, $\bar{v}_2$=0 m/s, (b) $g' = 1.5 \cdot 10^{-2}$ m/s^2, $\bar{v}_1$=0.3 m/s, $\bar{v}_2$=0 m/s, (c) $g' = 0.5 \cdot 10^{-2}$ m/s^2, $\bar{v}_1$=0.2 m/s, $\bar{v}_2$=0.05 m/s, (d) $g' = 1.5 \cdot 10^{-2}$ m/s^2, $\bar{v}_1$=0.2 m/s, $\bar{v}_2$=0.05 m/s. The analytical dispersion relation of the internal gravity wave (flat bottom) is also shown (black line).

In Figure 7, the theoretical semi-circles (equation 8) that bound the eigenmodes corresponding to the cases in Figure 6a-d are plotted, along with the complex phase speed of the unstable modes calculated with the present model. All the modes lie within the semi-circle, which gives an independent indication that the numerical results are sound, although the semi-circle theorem is derived for a flat bottom.

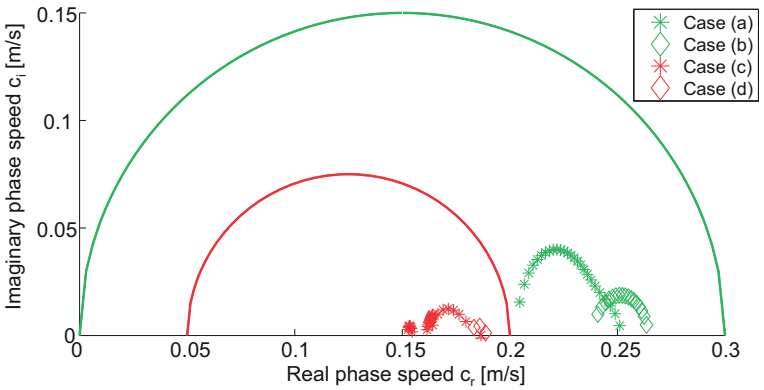

Figure 7: The semi-circles (8) corresponding to $\bar{v}_1$=0.3 m/s, $\bar{v}_2$=0 m/s (green) and $\bar{v}_1$=0.2 m/s, $\bar{v}_2$=0.05 m/s (red). The unstable modes calculated with the present model for cases (a-d) in Figure 6 are indicated.

A sensitivity analysis was carried out to evaluate any systematic deviations between the present model and that of Mysak and Schott [1977]. In Figure 8a and b, the sensitivity to the magnitude of the current speed in either layer is shown. Some general observations can be made from this plot. The growth rate increases with increasing shear between the two layers, which is to be expected from standard theory of baroclinic instability, see e.g. [Smith, 2007], who derived an expression where the growth rate is proportional to the inverse square root of the bulk Richardson number (Ri), $\gamma \propto \frac{1}{\sqrt{Ri}} = \frac{\bar{v}_1 - \bar{v}_2}{\sqrt{g'd}}$. The model of Mysak and Schott [1977] is generally giving slightly higher wave periods and growth rates than the present model. In Figure 8c and d, the sensitivity to changes in bottom slope and reduced gravity are investigated. The growth rate is increasing, while the wave period and wave length are decreasing, with weakening stratification. This is in line with the condition given in equation 9, where the third term will dominate for strong stratification and/or topographic slopes, rendering instability less likely. An increasing topographic slope is decreasing the growth rate, wave period and wave length. In all the cases in Figure 8a-d, the qualitative similarity between the two models is obvious, although the present model seem to produce slightly lower growth rates.

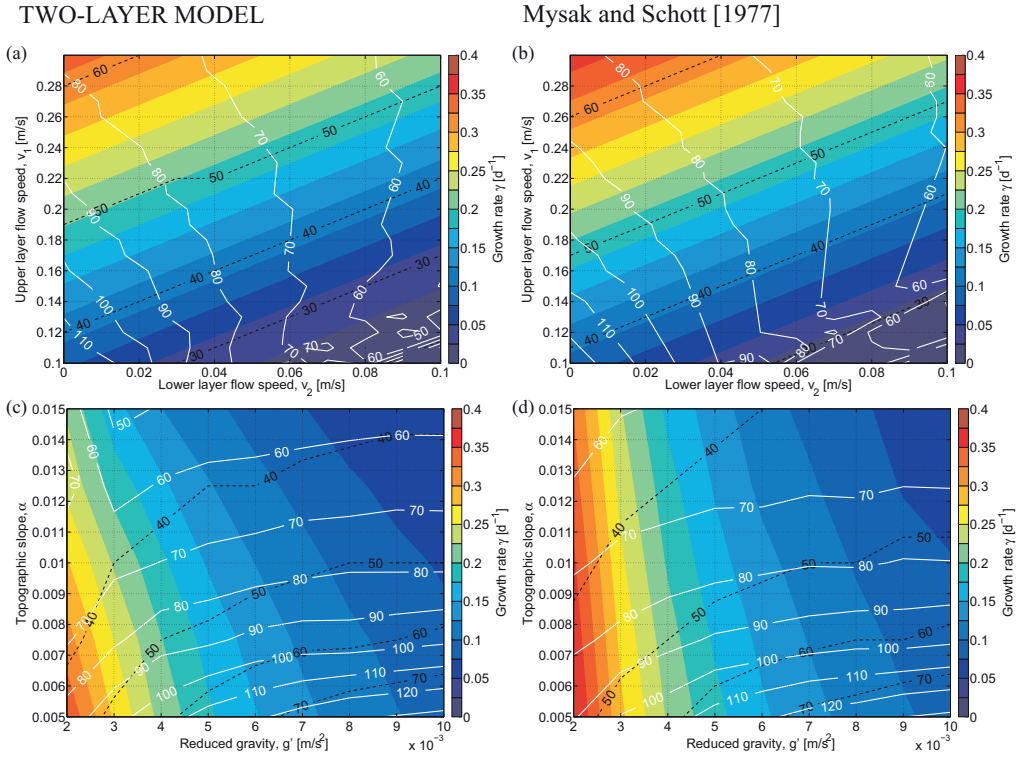

Figure 8: In the two upper panels, a sensitivity study of the upper and lower layer flow speed with the present model (a) and that of Mysak and Schott [1977] (b) is presented. In the two lower panels, the sensitivity of the bottom slope and reduced gravity with the present model (c) and that of Mysak and Schott [1977] (d) is shown. The growth rate of the gravest unstable mode is plotted with colored, filled contours, whereas the corresponding period of the gravest unstable mode is displayed with white, labeled contour lines. The wavelength of the gravest unstable mode is shown with black, dotted contour lines.

4.3 Case study: the West Spitsbergen Current

The modeled West Spitsbergen topography is uniform in the along-shelf direction, and the undisturbed water depth, $h(x)$, is represented by a smooth double tanh function in the across-shelf direction (resolving the two-step nature of the slope, see the illustration in Figure 9)

$$h(x) = a_1\left(1 - g_1 \tanh\left(\frac{x - x_1}{s_1}\right)\right) + a_2\left(1 - g_2 \tanh\left(\frac{x - x_2}{s_2}\right)\right) - a_2(1 - g_2), \qquad (14)$$

where $a_1 = 621$ m, $g_1 = 0.7069$, $x_1 = 117$ km, $s_1 = 7$ km, $a_2 = 2350$ m, $g_2 = 0.3191$, $x_2 = 155$ km and $s_2 = 14$ km. This is the same bathymetric function as was used by Nilsen *et al.* [2006] and

Teigen *et al.* [2010]. The maximum upper bottom slope is $\sim 6 \cdot 10^{-2}$ and somewhat steeper than the maximum deep bottom slope ($\sim 5 \cdot 10^{-2}$). The more gently sloping segment between the two slopes is $\sim 1 \cdot 10^{-2}$. For the West Spitsbergen configuration, the density interface between the two layers intersects the bottom topography, resulting in an offshore two-layer region and an onshore mono-layer region. The background current field in both layers is modelled as a Gaussian jet, given by

$$\bar{v}_n(x) = \bar{v}_{0,n} \exp\left[-\left(\frac{x - L_B}{B}\right)^2\right], n = 1, 2. \tag{15}$$

Here, L_B is the position of the current maximum, while $\bar{v}_{0,n}$ is the maximum current speed in layer n and B is the half-width of the jet. L_B and B are assumed to be the same in the two layers.

Three different calculation domains were considered (see Figure 9) for the numerical computations. Case I includes the flat, deep portion of the channel ($x = 0$ km) to the shelf-break ($x = 165$ km), Case II consists merely of the slope (from the foot of the slope, $x = 65$ km, to the shelf-break, $x = 165$ km), while Case III spans the deep portion, slope and shelf ($x = 0$ km to $x = 300$ km). The three cases were run with the input values given in Table 5, for three different grid sizes ($\Delta x = 1, 0.5, 0.25$ km).

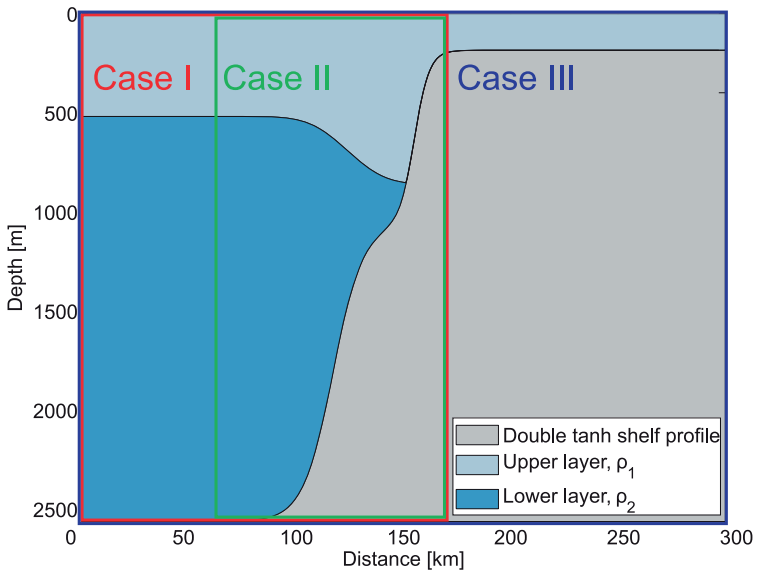

Figure 9: Illustration of the West Spitsbergen Slope and the three calculation domains that were tested.

In Table 6, the mode with the highest growth rate is tabulated for the three different domains and the different grid sizes. As can be seen, it is not possible to distinguish between Case I and II, hence excluding the flat interior of the channel does not seem to affect the properties of the gravest unstable mode to any notable extent. There are some differences between the solution for

Table 5: Input parameters, West Spitsbergen shelf

Parameter	Value
$\bar{v}_{0,1}$	0.20 m/s
$\bar{v}_{0,2}$	0.05 m/s
L_B	124 km
B	20 km
g'	0.0022 m/s^2
d	840 m
f	$1.42{\cdot}10^{-4}$ s^{-1}

Case I-II and Case III (including the shelf) that should be remarked. For Case III, the maximum growth rate occurs at longer (2-3 km) wavelengths and wave periods (7-8 h), and at considerably lower growth rate (3 times lower). For a grid size of $\Delta x = 1$ km, the mode with the highest growth rate for Case III appears at much shorter (12.5 km) wavelength, indicating that Case III is more sensitive to numerical resolution than the other two cases. The modal structure of this mode is concentrated shoreward of the shelf-break in the upper layer and is limited to a narrow region close to the intersection between the layer interface and the slope in the lower layer. In Figure 10a and b, the detailed dispersion relations for Case II and III are shown, respectively (for grid size $\Delta x = 0.5$ km). An immense number of stable and unstable modes can be seen, compared with the basic dispersion relation for the linear shelf and uniform current in section 4.2. The increased complexity is due to the introduction of cross-shelf variation in bottom slope and current, allowing for a rich variety of cross-modal interactions. For Case II, two distinct peaks in growth rate step out ($\lambda = 27.5$ km, $T = 50$ h, $\gamma = 0.11$ d^{-1} and $\lambda = 35$ km, $T = 68$ h, $\gamma = 0.05$ d^{-1}). The same peaks can be discerned for Case III as well, but they are shifted towards longer wave lengths and the second peak is more diffuse. The maximum growth rates are also greatly reduced. When displayed in wave length/phase speed space (Figure 10c and d), the dispersion diagram becomes more lucid, the dominant peaks in growth rate appearing along linear bands of unstable modes. For Case II (Figure 10c), the two dominant peaks in growth rate are clearly visible. The resulting phase speed of the most unstable mode is quite similar for the two cases, 0.152 m/s for Case II and 0.146 m/s for Case III. There are two regions where the density of modes is especially high. These modes have phase speeds close to either the upper or the lower layer's maximum speed, and are characterised as surface- or bottom-intensified modes Mysak [1980] (the gray shaded regions in Figure 10c and d).

Table 6: Evaluation of calculation domain for the WSSl. γ is growth rate with unit [days^{-1}].

			λ [km]/T [h]/γ [days^{-1}]		
Case	$x_{\mathbf{start}}$ [km]	$x_{\mathbf{end}}$ [km]	$\Delta x = 1.0$ km	$\Delta x = 0.5$ km	$\Delta x = 0.25$ km
I	0	165	28/50.46/0.110	27.5/50.21/0.109	27.5/50.17/0.109
II	65	165	28/50.46/0.110	27.5/50.21/0.109	27.5/50.17/0.109
III	0	300	12.5/90.06/0.045	30.5/58.09/0.039	30.5/57.98/0.036

An additional test was run for Case II and III, in which the maximum speed in the upper layer

was increased to $\bar{v}_{0,1} = 0.35$ m/s (the other parameters were kept the same as in Table 5). For this case of stronger shear the resulting peak in growth rate for the two cases turned out to be quite similar (see Table 7), Case III displaying 5% less growth rate, 4% longer wave length and 10% higher wave period than Case II. This corresponds well with the findings of Mysak *et al.* [1981], who found that the characteristics of the dominant baroclinically unstable wave differed little for a channel model and a shelf model. To summarize, including the shelf region makes the solution less numerically robust for moderate shears in the present model formulation. This is manifested in the growth rates, which are more sensitive to grid size for Case III (see Table 6). For applications that focus on the physics of instabilities over the slope, it is preferable to limit the extent of the calculation domain to the slope region. This is also beneficial for saving computational time.

Table 7: Peak in growth rate for stronger shear, $\bar{v}_{0,1} = 0.35$ m/s. γ is growth rate with unit [days^{-1}].

Case	$x_{\mathbf{start}}$ [km]	$x_{\mathbf{end}}$ [km]	λ [km]/T [h]/γ [days^{-1}] $\Delta x = 0.5$ km
II	65	165	36/46.66/0.419
III	0	300	37.5/51.53/0.399

For a moderate shear ($\bar{v}_{0,1} = 0.2$ m/s, $\bar{v}_{0,2} = 0.05$ m/s), the upper and lower layer modal structures associated with the highest peak ($T = 50$ h) in growth rate are plotted in Figure 11 for Case II. The centre of the vorticity wave in the upper layer is located close to the position of the maximum vertical current shear. In the lower layer, the vorticity structure extends all the way to the intersection between the layer interface and the continental slope. In Figure 12, the upper and lower layer modal structures associated with the second ($T = 68$ h) peak in growth rate are plotted. A dipole structure can be seen, with vorticity centers both east and west of the maximum vertical current shear. The easterly vorticity centre is more energetic than the others in the upper layer, while in the lower layer they are more similar in strength. In the lower layer, the wave structure is cell-like and the oscillation is intensified at the intersection between layer interface and the shelf slope.

5 Conclusions

A shallow-water two-layer model for analysis of stable and unstable modes in shelf-slope currents has been implemented. The model shows good agreement with analytical results, and can be applied for a wide range of shelf and current profiles. Results from the model can be helpful in the analysis of current meter data on shelf-slopes and results from numerical ocean models. The present model may also be used in conjunction with the more general Brink model [Brink, 2006], which requires a-priori knowledge about the modes one is searching for, but allows for continuous stratification.

6 Acknowledgement

I wish to thank Professor B. Gjevik at the at the University of Oslo (Department of Mathematics) for many stimulating discussions and valuable suggestions for this report.

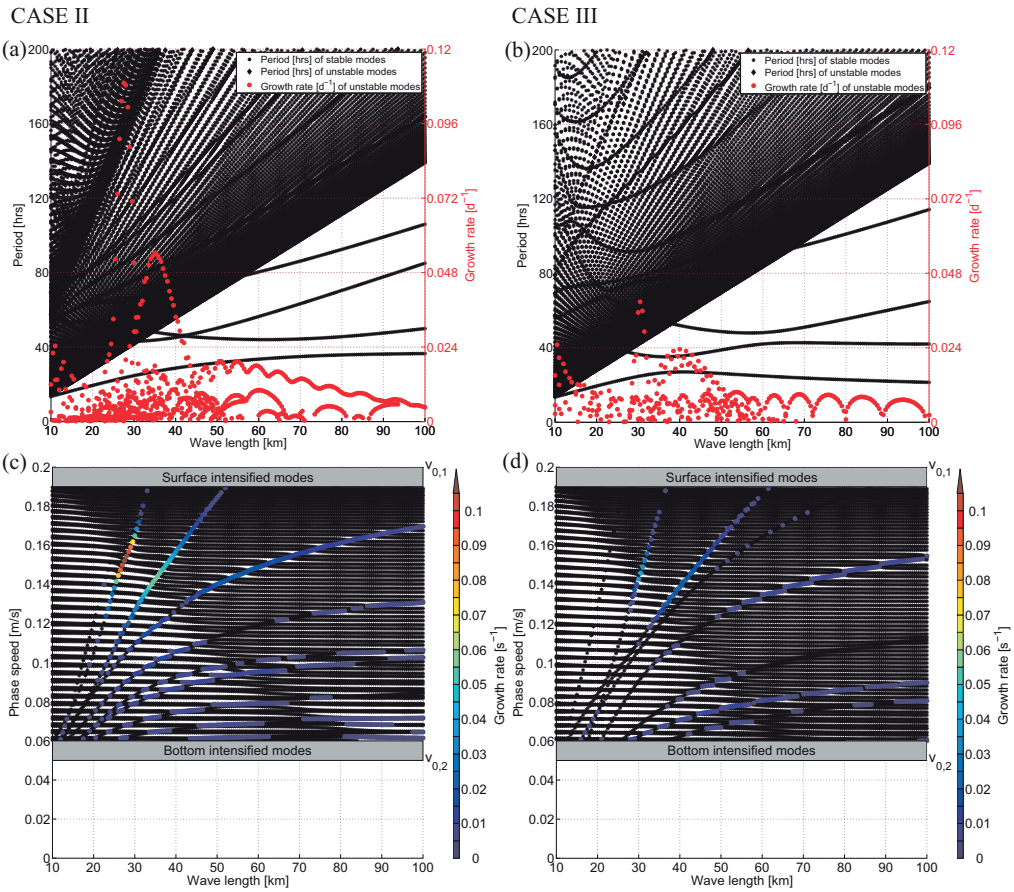

Figure 10: Dispersion diagrams for Case II and III with $\Delta x = 0.5$ km. (a) and (b) are plotted with wave period on the y-axis, while (c) and (d) is depicted with phase speed on the y-axis. The period of both stable (black asterisks) and unstable modes (black diamonds) are shown.

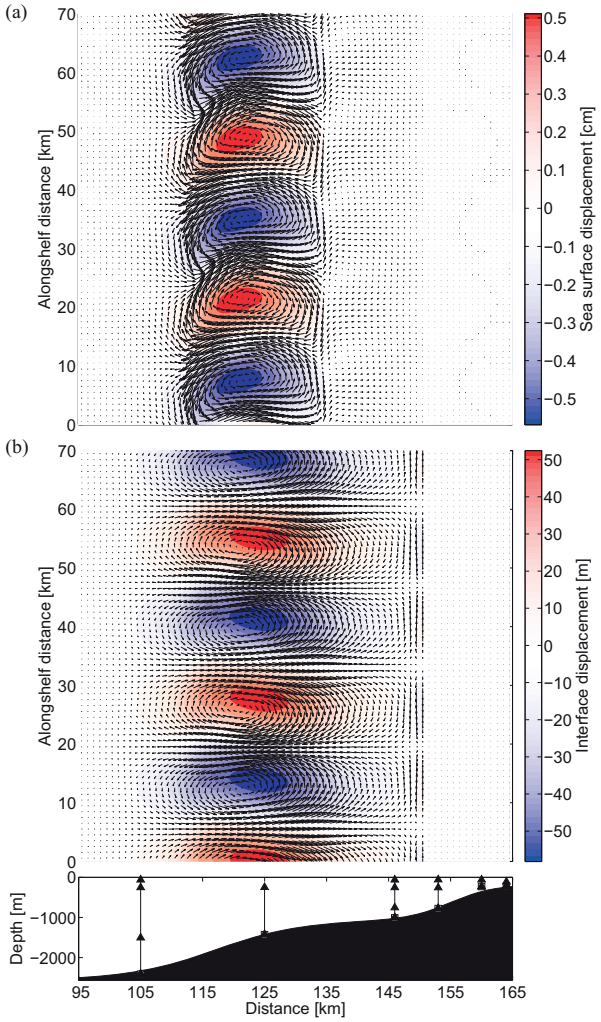

Figure 11: (a) Upper layer modal structure of the unstable wave mode corresponding to the first peak in growth rate ($\lambda = 28$ km, $T = 50$ h). The perturbation flow field is shown with black vector arrows. The perturbation sea surface displacement is plotted in red/blue. (b) Lower layer modal structure. The perturbation interface displacement is plotted in red/blue.

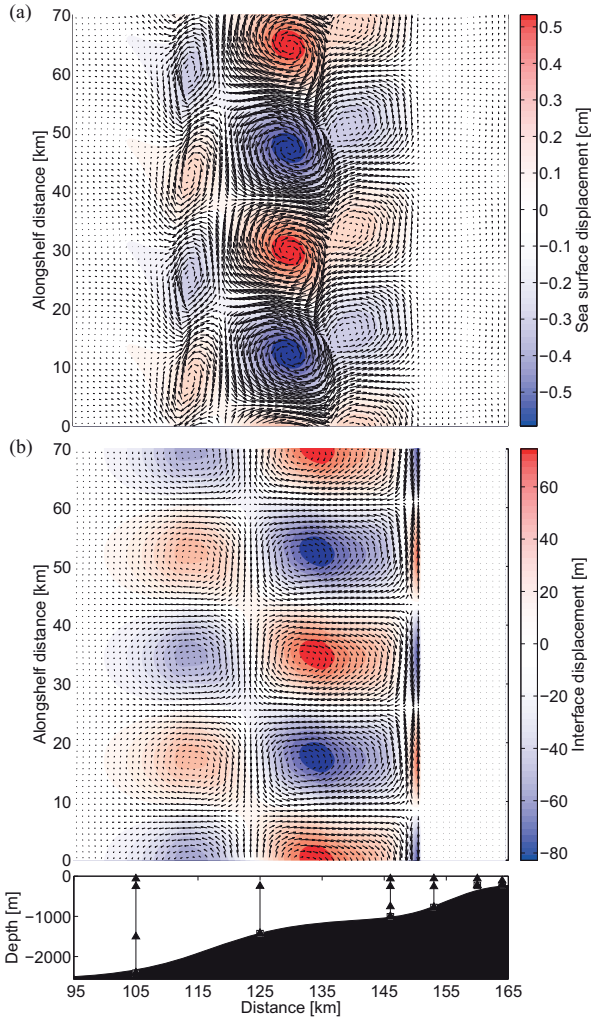

Figure 12: (a) Upper layer modal structure of the unstable wave mode corresponding to the second peak in growth rate ($\lambda = 35$ km, $T = 68$ h). The perturbation flow field is shown with black vector arrows. The perturbation sea surface displacement is plotted in red/blue. (b) Lower layer modal structure. The perturbation interface displacement is plotted in red/blue.

References

Boyd, T. J. and D'Asaro, E. A. (1994). Cooling of the West Spitsbergen Current: Wintertime Observations West of Svalbard. *J. Geophys. Res.*, **99**(C11), 22597–22618.

Brink, K. H. (2006). Coastal-trapped waves with finite bottom friction. *Dyn. Atm. Ocean*, **41**, 172–190.

Charney, J. G. (1947). The Dynamics of Long Waves in a Baroclinic Westerly Current. *J. Meteor.*, **4**(5), 136–162.

Davies, A. M., Xing, J., and Gjevik, B. (2003). Barotropic eddy generation by flow instability at the shelf edge: Sensitivity to open boundary conditions, inflow and diffusion. *J. Geophys. Res.*, **108**(C2).

Eady, E. T. (1949). Long Waves and Cyclone Waves. *Tellus*, **1**, 33–52.

Ferrari, R. and Wunsch, C. (2009). Ocean Circulation Kinetic Energy: Reservoirs, Sources, and Sinks. *Annu. Rev. Fluid Mech.*, **41**, 253–282.

Flierl, G. R. (1978). Models of vertical structure and the calibration of two-layer models. *Dyn. Atmos. Ocean*, **2**, 341–381.

Gascard, J.-C., Richez, C., and Rouault, C. (1995). New insights on large-scale oceanography in Fram Strait: the West Spitsbergen Current. *Cont. Shelf Res.*, **49**, 131–182.

Gill, A., Green, J., and Simmons, A. (1974). Energy partition in the large-scale ocean circulation and the production of mid-ocean eddies. *Deep Sea Res.*, **21**(7), 499 – 508, IN1, 509–528.

Gjevik, B. (2002). Unstable and neutrally stable modes in barotropic and baroclinic shelf slope currents. Preprint Series 1, Dept. of Mathematics, Univ. of Oslo, Oslo, Norway.

Howard, L. N. (1961). Note on a paper of John W. Miles. *J. Fluid Mech.*, **10**, 509–512.

Ikeda, M. (1983). Linear Instability of a Current Flowing Along a Bottom Slope Using a Three-Layer Model. *J. Phys. Oceanogr.*, **13**(2), 208–223.

Isachsen, P. E. (2010). Baroclinic instability and eddy tracer transport across sloping bottom topography: How well does a modified Eady model do in primitive equation simulations? *Ocean Modell.*, **In Press, Corrected Proof**.

Johannessen, J. A., Johannessen, O. M., Svendsen, E., Shuchman, R., Manley, T., Campbell, W. J., Josberger, E. G., Sandven, S., Gascard, J. C., Olaussen, T., Davidson, K., and Leer, J. V. (1987). Mesoscale Eddies in the Fram Strait Marginal Ice Zone During the 1983 and 1984 Marginal Ice Zone Experiments. *J. Geophys. Res.*, **92(C7)**, 6754–6772.

Kawabe, M. (1982). Coastal Trapped Waves in a Two-layer Ocean: Wave Properties When the Density Interface Intersects a Sloping Bottom. *J. Oceanogr. Soc. Japan*, **38**(3), 115–124.

Mysak, L. A. (1980). Recent advances in shelf wave dynamics. *Rev. Geophys.*, **18**(1), 211–241.

Mysak, L. A. and Schott, F. (1977). Evidence for baroclinic instability of the Norwegian Current. *J. Geophys. Res.*, **82**(15), 2087–2095.

Mysak, L. A., Muench, R. D., and Schumacher, J. D. (1981). Baroclinic Instability in a Downstream Varying Channel: Shelikof Strait, Alaska. *J. Phys. Oceanogr.*, **11**(7), 950–969.

Nilsen, F., Gjevik, B., and Schauer, U. (2006). Cooling of the West Spitsbergen Current: Isopycnal diffusion by topographic vorticity waves. *J. Geophys. Res.*, **111**, 1–16.

Orlanski, I. (1969). The influence of Bottom Topography on the Stability of Jets in a Baroclinic Fluid. *J. Atm. Sci.*, **26**(6), 1216–1232.

Pedlosky, J. (1963). Baroclinic instability in two layer systems. *Tellus*, **15**(1), 20–25.

Pedlosky, J. (1964a). The Stability of Currents in the Atmosphere and the Ocean: Part i. *J. Atm. Sci.*, **21**(2), 201–219.

Pedlosky, J. (1964b). The Stability of Currents in the Atmosphere and the Ocean: Part ii. *J. Atm. Sci.*, **21**(4), 342–353.

Phillips, N. A. (1954). Energy Transformations and Meridional Circulations associated with simple Baroclinic Waves in a two-level, Quasi-geostrophic Model. *Tellus*, **6**, 273–286.

Pichevin, T. (1998). Baroclinic instability in a three layer flow: a wave approach. *Dyn. Atm. Oceans*, **28**(3-4), 179 – 204.

Poulin, F. J. and Flierl, G. R. (2005). The influence of topography on the Stability of Jets. *J. Phys. Oceanogr.*, **35**, 811–825.

Smith, K. S. (2007). The geography of linear baroclinic instability in Earth's oceans. *J. Mar. Res.*, **65**, 655–683.

Smith, P. C. (1976). Baroclinic Instability in the Denmark Strait Overflow. *J. Phys. Oceanogr.*, **6**(3), 355–371.

Teigen, S. H., Nilsen, F., and Gjevik, B. (2010). Barotropic Instability in the West Spitsbergen Current. *J. Geophys. Res.*, **115**, C07016.

Thiem, O., Berntsen, J., and Gjevik, B. (2006). Development of eddies in an idealised shelf slope area due to an along slope barotropic jet. *Cont. Shelf Res.*, **26**(12-13), 1481 – 1495.